Correspondence

Application of a Real-Time, Calculable Limiting Form of the Renyi Entropy for Molecular Imaging of Tumors

Jon N. Marsh, *Member, IEEE*, Kirk D. Wallace, *Member, IEEE*, John E. McCarthy, Mladen V. Wickerhauser, Brian N. Maurizi, Gregory M. Lanza, *Member, IEEE*, Samuel A. Wickline, *Member, IEEE*, and Michael S. Hughes

***Abstract*—Previously, we reported new methods for ultrasound signal characterization using entropy, H_f; a generalized entropy, the Renyi entropy, $I_f(r)$; and a limiting form of Renyi entropy suitable for real-time calculation, $I_{f,\infty}$. All of these quantities demonstrated significantly more sensitivity to subtle changes in scattering architecture than energy-based methods in certain settings. In this study, the real-time calculable limit of the Renyi entropy, $I_{f,\infty}$, is applied for the imaging of angiogenic murine neovasculature in a breast cancer xenograft using a targeted contrast agent. It is shown that this approach may be used to reliably detect the accumulation of targeted nanoparticles at five minutes post-injection in this *in vivo* model.**

I. Introduction

In previous work, we have described the use of a targeted nanoscale contrast agent for use with magnetic resonance imaging, X-ray, and ultrasound. In this application, $\alpha_v\beta_3$-targeted perfluorocarbon core nanoparticles are injected into the blood stream where they circulate and accumulate at angiogenic sites that are associated with advancing fronts of growing tumors. The geometry of this angiogenic neovasculature is highly convoluted, and the targeting sites sparse, so that the accumulating nanoparticles never comprise a planar specular reflector. Consequently, a scheme capable of sub-resolution sensitivity is required for their detection.

Sub-resolution detection has a long history and has typically been based on statistical signal processing using Gaussian, Rayleigh, or Rician statistics [1]–[8]. The technique we investigate in this study utilizes an approach formulated with a significantly different underlying mathematical structure [9]. It is based on the use of various forms of entropy analysis for the detection of perfluorocarbon nanoparticles targeted to tumor neovasculature [10]–[13]. These quantities are computed using a density function determined by each individual RF A-line considered as a noise-free (or nearly so) measurable function [14]. All measurable functions, not just noise functions, have mathematically well-defined distributions (because they are all random variables), which may be used to compute any one of several entropies. We have found that the use of these novel information-theoretic receivers is often advantageous for overcoming certain challenges related to acoustic characterization of sparse collections of nanoparticles. The physically robust liquid perfluorocarbon nanoparticles are intrinsically weak individual scatterers in the clinical ultrasound frequency range because of their small size and nongaseous nature, and are typically targeted to physiological features at interfaces having inherent impedance mismatches (e.g., vessel walls). In addition, the epitopes to which they are targeted may be sparsely located in the accessible vasculature. Entropy techniques are well-suited to detecting small changes in the shape of the backscattered RF waveforms which may be masked by other strongly scattering features when using typical energy-based analyses. The end goal is to enable detection of nanoparticles accumulating at epitopes of interest in the least amount of time after administration, with a view toward demonstrating sensitivity to smaller quantities of contrast agent, thereby potentially reducing patient discomfort and increasing clinical throughput.

The *in vivo* studies in which we have utilized these techniques typically entail intravenous injection of nanoparticles that are targeted to angiogenic markers present in cancerous or precancerous tissue. The tumor site is monitored ultrasonically as the contrast agent circulates, and backscattered RF waveforms are acquired at specific time points for entropy analysis. Initial studies showed that a limiting form, H_f, of the Shannon entropy, H_S, enabled detection of nanoparticle accumulation at 30 min post-injection in a mouse model of squamous metaplasia [11]. Subsequent work demonstrated that a generalized form of entropy, the Renyi entropy $I_f(r)$, could be used to distinguish backscatter differences from the previously acquired data at only 15 min post-injection [12]. $I_f(r)$, where r may be thought of as a reciprocal temperature in the statistical mechanics sense, is defined for all $r < 2$; the improved detection results were obtained with $r = 1.99$.

Although the computational effort to obtain these results precluded clinical application with currently available equipment, the study raised the possibility of further sensitivity improvements by using values of r closer to the limiting value of 2, where $I_f(r)$ approaches infinity. Further work based on this limiting form, labeled $I_{f,\infty}$, confirmed its utility for rapid detection of nanoparticle targeting in the same animal model [13]. Moreover, the implementation of the algorithm used to compute $I_{f,\infty}$ was much less computationally intensive, having an operation

Manuscript received January 29, 2010; accepted April 15, 2010. This study was funded by NIH EB002168, HL042950, and CO-27031 and NSF DMS 0501079. The research was carried out at the Washington University Department of Mathematics and the School of Medicine.

J. E. McCarthy and M. V. Wickerhauser are with the Department of Mathematics, Washington University in St. Louis, St. Louis, MO.

J. N. Marsh, K. D. Wallace, G. M. Lanza, S. A. Wickline, and M. S. Hughes are with the School of Medicine at Washington University in St. Louis (e-mail: jnm@cvu.wustl.edu).

Digital Object Identifier 10.1109/TUFFC.2010.1630

0885–3010/$25.00 © 2010 IEEE

Authorized licensed use limited to: WASHINGTON UNIVERSITY LIBRARIES. Downloaded on July 21,2024 at 15:56:06 UTC from IEEE Xplore. Restrictions apply.

count lower than that used to produce the signal envelope (currently the standard for real-time ultrasonic imaging display), thus demonstrating its suitability for implementation in a real-time imaging system. Because this technique is based on a moving window analysis of digitized RF (which requires some sacrifice in spatial resolution), clinical implementation of entropy detection would probably follow the same approach currently employed in color Doppler or strain-rate imaging modalities, in which the conventional B-mode image is overlaid with a color-coded mapping; a B-mode/entropy image could be constructed in a similar fashion.

We now present new data acquired from a murine tumor model injected with nanoparticles targeted to the $\alpha_v\beta_3$ integrin, a marker for angiogenesis. Ultrasonic data are acquired on a finer time scale (every 5 min over the course of 1 h) to further delineate the efficacy of entropy analysis for both sensitive and specific detection of nanoparticle accumulation in and around the tumor capsule. The results of this analysis are compared, using various statistical criteria, with corresponding conventional energy-based measures applied to the same data.

II. Approach

All entropy results in this study were obtained using

$$I_{f,\infty} = \log\left[\sum_{\{t_k|f'(t_k)=0\}} \frac{1}{|f''(t_k)|}\right], \tag{1}$$

which is derived from an asymptotic analysis of the Renyi entropy I_f ($r \to 2$), as described previously [13]. In this application, $f(t)$ refers to an individual RF waveform, $f'(t)$ and $f''(t)$ are its first and second derivatives with respect to time, and t_k is the time at which the kth extremum occurs. Previous studies have shown that this quantity [i.e., $I_{f,\infty}$, as well as $I_f(r)$ and H_f, which is a generalization of $I_f(r)$] can be more sensitive to subtle changes in scattering architecture than more commonly used energy-based measures [11]–[13]. We base our current study exclusively on $I_{f,\infty}$, because this quantity is calculable in real-time as described previously [13].

III. Materials and Methods

A. Animal Model

The study was performed according to an approved animal protocol and in compliance with guidelines of the Washington University institutional animal care and use committee.

Human MDA435 cancer cells were implanted in the inguinal fat pad of fifteen athymic nude mice between 19 and 20 d before acquisition of data. After this period of tumor growth, five of these animals were injected with $\alpha_v\beta_3$-targeted nanoparticles, five were injected with non-targeted nanoparticles, and five were injected with saline.

Prior to imaging, each mouse was pre-anesthesitized with a ketamine/xylazine cocktail, and injected subsequently through the tail vein with either 30 μL of $\alpha_v\beta_3$-targeted nanoparticle emulsion, 30 μL of non-targeted nanoparticle emulsion, or 30 μL of saline (equivalent to a whole body dose of 1.0 mL/kg; the preparation and properties of these emulsions have been described previously [12], [13]). The mouse was then placed on a heated platform maintained at 37°C, and anesthesia was administered continually with isoflurane gas through a nose cone. Post-injection, ultrasound data were acquired at 5-min intervals for 1 h. After the ultrasound data were collected, the mouse was killed and the tumor was excised for histological staining.

B. Ultrasonic Data Acquisition

A schematic of the experimental setup is shown in Fig. 1. RF data were acquired with a research ultrasound system (Vevo 660, Visualsonics, Toronto, Canada) having analog and sync ports to permit digitization. Tumors were located and imaged with a 35-MHz single element probe, and the RF data corresponding to single frames were stored for off-line analysis. Each frame consisted of 384 lines of 2048 twelve-bit words acquired at a sampling rate of 200 MHz using a CompuScope 12400 digitizer card (GaGe Applied Technologies, Lockport, IL) in a controller PC. Each frame corresponded spatially to a region 1.5 cm wide and 0.8 cm deep. At the bottom left of Fig. 1 is a conventionally formed image from one of the mice used in our study. Also shown in this figure is a representative histological section extracted from an example mouse model. Visible in the section is an area of skin, below which is a thin angiogenic layer identified by immunohistochemical staining, and below that, a portion of the tumor capsule. The close proximity of neovasculature to the skin-transducer interface is one of the primary obstacles that must be overcome by any quantitative detection scheme intended to determine the extent of this region.

C. Ultrasonic Image Preparation and Processing

Because the real-time entropy depends on the second derivative of the raw data, a potentially noise-enhancing process, all RF data were lowpass-filtered in the frequency domain as a first step in data analysis. This was accomplished by multiplying the Fourier transform of each RF line by the filter function, $F(f)$,

$$F(f) = \frac{1}{2}(1.0 + \tanh[a(f_c - f)]), \tag{2}$$

where $a = 0.25$ and $f_c = 36$ MHz. The cutoff frequency f_c was chosen to correspond to the typical upper limit of the meaningful bandwidth of the backscattered signal from within the tumors after being attenuated by overlying tissue. The function $F(f)$ has the shape of a smoothed rectangular window whose passband drops off near f_c. The

Authorized licensed use limited to: WASHINGTON UNIVERSITY LIBRARIES. Downloaded on July 21,2024 at 15:56:06 UTC from IEEE Xplore. Restrictions apply.

coefficient a governs the sharpness of this transition. This function was chosen as a gate function because it is infinitely differentiable. We have investigated other window functions (e.g., various pole-number Butterworth filters) and find that all perform in a roughly equivalent way. The use of other types of noise suppression, such as the application of smoothing splines to the input RF waveforms, is an active area of research in our laboratory whose impact is currently being assessed.

After filtering, each of the 384 RF lines in the frame was first up-sampled from 2048 to 4096 points, using a cubic spline fit to the original data set to improve the stability of the entropy algorithms. A by-product of this order-N (where N is the number of sample points) algorithm is simultaneous output of a corresponding array of second derivative values of the fit function [15]. Next, a moving window analysis was performed on the second derivative data set, using (1) to compute $I_{f,\infty}$, by translating a rectangular window (256 points long, 0.64 μs) in 0.08-μs steps (32 points), resulting in 121 window positions within the output data set. For comparison, an analogous procedure was performed on the same data using a conventional imaging metric, based on the logarithm of the signal energy ($\log[E_f]$).

Grayscale images formed from the processed data were subjected to an image-histogram based analysis to quantify levels of enhancement, beginning with computation of the normalized probability density function (PDF) of the image sequence (i.e., 0-, 5-, ..., 60-min images). The PDF was then integrated to obtain the cumulative distribution function (CDF) of the image sequence. The pixel values corresponding to the lower 2%, 4%, ..., 98% of the CDF were then used to segment each image in the sequence into two regions corresponding to enhanced and unenhanced tissue. The mean value of pixels in the enhanced region was computed for each image in the sequence as a function of time post-injection. Beyond the initial selection of the imaging plane and digitization window, no user-drawn regions of interest were utilized in the image analysis, all digitized signals were included.

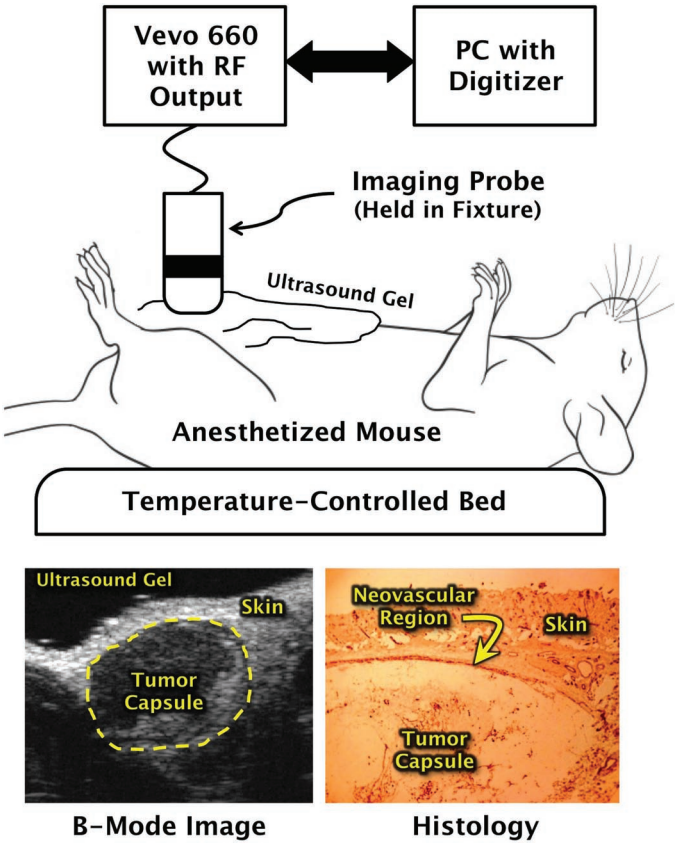

Fig. 1. Top: Schematic diagram of the equipment used to acquire *in vivo* backscattered RF data. Bottom panels show example B-mode ultrasound image of tumor (left) and a stained histologic section of a tumor indicating portions where $\alpha_v\beta_3$-targeted nanoparticles could adhere (right).

IV. Results and Discussion

Fig. 2 shows the average change in $I_{f,\infty}$ (relative to the first observation point, which was typically acquired within 1 min of nanoparticle injection) for the animals used in this study labeled in each plot by group. Error bars are also shown at each time point. These plots were obtained using the $I_{f,\infty}$ image segmented by setting the CDF threshold to include only the bottom 30% of $I_{f,\infty}$ pixel values. The top panel shows the plot for the animals injected with $\alpha_v\beta_3$-targeted nanoparticles, which decreases as a function of time. The downward trend is less evident for both the non-targeted and saline control groups. It should be noted that the trend for decreasing $I_{f,\infty}$ values with time is opposite of what has been reported in a different model of cancer growth, the K14-HPV16 precancerous mouse ear analyzed with a variety of information-theoretic metrics [11]–[13]. Although it is not clear what effect the difference in tissue type might produce, we note that there is substantially more attenuation associated with ultrasound backscattered from the thicker and deeper tissue regions of the solid tumors described here than with the very thin ears of the previous studies. Although not reported here, we have observed that altering the spectral content of the input waveforms via filtering or other means can change the direction of the temporal trends seen in $I_{f,\infty}$ from negative to positive, or vice versa; however, the differences between targeted and control groups are typically preserved, and it is these differences that are important for reliable detection of accumulating nanoparticles.

The average plot for the group injected with $\alpha_v\beta_3$-targeted nanoparticles is reproduced on the left side of Fig. 3. The right side of the figure shows a plot of the corresponding ratio of the mean value to standard error for each time point. For the purposes of detecting a change from the baseline value, it is actually this ratio that is important. To shorten subsequent discussion of our results we will define this ratio, labeled the confidence, or c [16]:

$$c = \frac{|\text{mean}|}{\text{standard error}}. \tag{3}$$

Authorized licensed use limited to: WASHINGTON UNIVERSITY LIBRARIES. Downloaded on July 21,2024 at 15:56:06 UTC from IEEE Xplore. Restrictions apply.

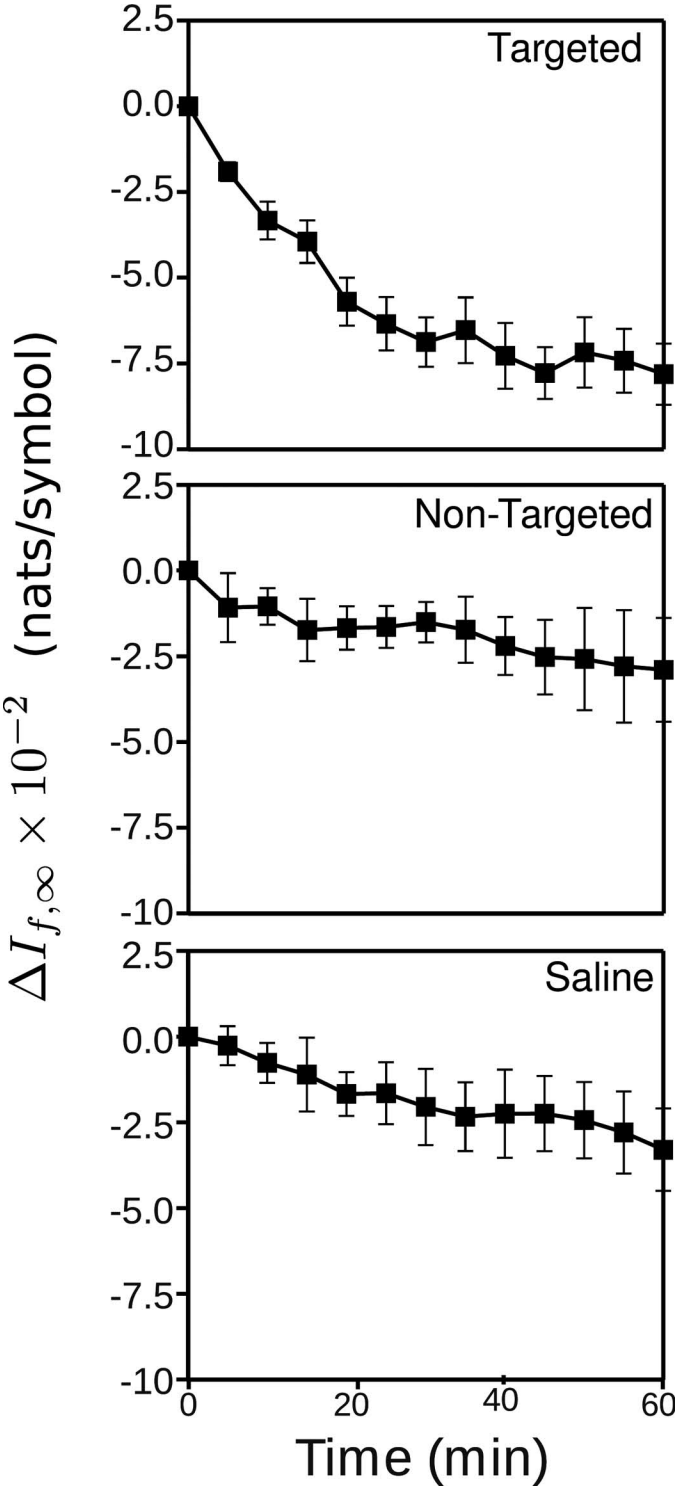

Fig. 2. Plots of the average change in $I_{f,\infty}$ with time for each group in this study, obtained by segmenting the $I_{f,\infty}$ images by setting the CDF threshold to include only the lowest 30% of pixel values.

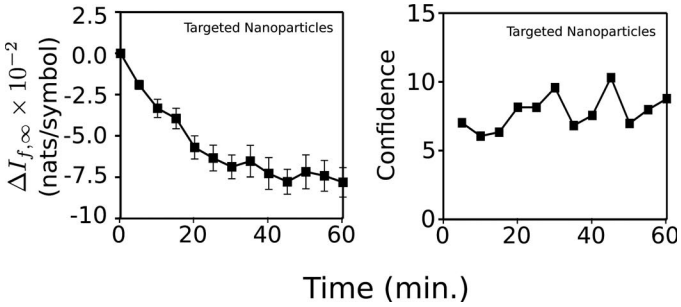

Fig. 3. Left: average time-course of $\Delta I_{f,\infty}$ images obtained from MDA435-implanted mice injected with $\alpha_v\beta_3$-targeted nanoparticles [same data shown in top of Fig. (2)]. Right: corresponding c values. These data were obtained with the CDF-threshold set to include the lower 30% of pixel values in the $I_{f,\infty}$ from each of the images in each group.

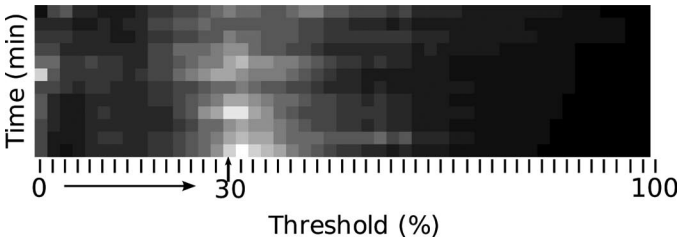

Fig. 4. Confidence values, c, plotted as a function of time and CDF threshold for tumor-implanted mice injected with $\alpha_v\beta_3$-targeted nanoparticles.

As stated previously, the analysis shown in Fig. 3 was performed for all even CDF-thresholds between 0 to 98%. A summary of all resulting confidence values for mice injected with $\alpha_v\beta_3$-targeted nanoparticles group is depicted as a gray-scale image in Fig. 4. The grayscale value in the image corresponds to the value of c, with brighter pixels signifying greater values of c. As the image shows, the greatest confidence values are obtained for a range of CDF-thresholds between roughly 2% and 50%. For reference, the column corresponding to the CDF-threshold of 30% that was discussed in Fig. 3 is indicated by an arrow and label.

The $I_{f,\infty}$ confidence images for all groups studied are shown in grayscale format in the top left half of Fig. 5. In the top right of the figure, identical images are shown, but with the overlay of a threshold mask to display only confidence values greater than 2.0; all other values have been colored red. The gray pixels represent the time/analysis-threshold combinations which are statistically significant by the two-sigma criterion. This threshold was chosen because it represents a common standard for statistical analysis, (i.e., 95% confidence interval). In the bottom half of the figure are shown the corresponding images for the $\log[E_f]$ receiver. For the conventions used in this study, the portion of the image selected by the segmentation increases as the analysis threshold is increased, so that at the 2% threshold very little of the image is selected for analysis, whereas at 98%, nearly all of the image is included. We note that the areas in the $I_{f,\infty}$-receiver panels for the group injected with $\alpha_v\beta_3$-targeted nanoparticles is somewhat larger than for the $\log[E_f]$ panel for the same group, indicating a broader range of analysis thresholds that imply the presence of accumulating targeted nanoparticles. This indicates that according to the two-sigma criterion, the $I_{f,\infty}$ receiver produces true positives over a broader range of analysis thresholds than does the $\log[E_f]$ receiver and is potentially a more robust statistic. Ad-

Authorized licensed use limited to: WASHINGTON UNIVERSITY LIBRARIES. Downloaded on July 21,2024 at 15:56:06 UTC from IEEE Xplore. Restrictions apply.

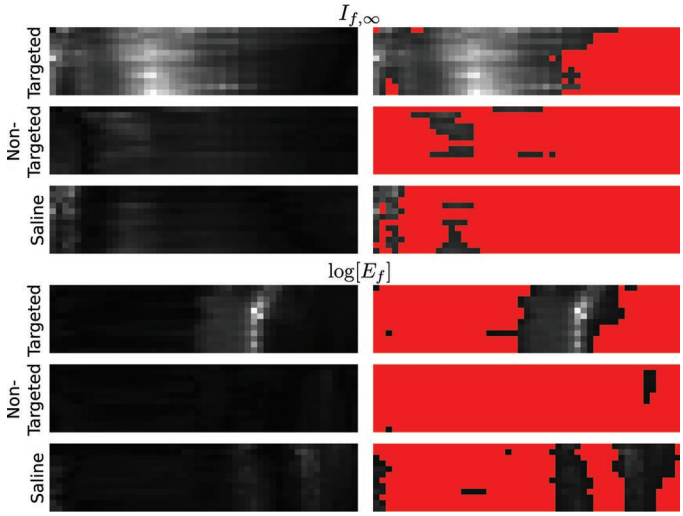

Fig. 5. Top left: a comparison of the confidence images for the $I_{f,\infty}$ receiver, like that shown in Fig. (4), for all groups in our study. Top right: the same data, but with all confidence values below 2 shown in red. Bottom left: a comparison of the confidence images for the $\log[E_f]$ receiver. Bottom right: the same data, with all confidence values below 2 shown in red.

ditionally, the total gray area in the control group panels (corresponding to non-targeted nanoparticle and saline injection) is less in the $I_{f,\infty}$ panels than in the $\log[E_f]$ panels, indicating a smaller number of false positives are produced by the $I_{f,\infty}$ receiver.

It is possible to formulate the detection problem in ways other than the two-sigma criterion. One of these is shown in Fig. 6, in which we have adjusted the thresholds of the confidence images to the minimum value required to eliminate false positives in the receiver outputs in the two control groups. For the $I_{f,\infty}$ receiver, this requires setting $c = 6.92$, for $\log[E_f]$, $c = 9.55$. As in Fig. 5, the gray pixels represent those time/analysis-threshold combinations at which statistical significance (by the no-false-positive criterion) is observed. We note that by this criterion the gray region is again larger for the $I_{f,\infty}$ receiver than it is for the $\log[E_f]$ receiver. Additionally, the presence of gray pixels in the top row of the $I_{f,\infty}$ confidence image indicates that detection of accumulating nanoparticles occurs within 5 min of particle injection (again, with no false positives), whereas the energy-based receiver registers a significant change only after 10 min of nanoparticle introduction. However, we point out that by both criteria we are able to successfully detect accumulation of targeted nanoparticles using either receiver.

V. Conclusion

Although both $I_{f,\infty}$ and $\log[E_f]$ are able to distinguish between the group injected with $\alpha_v\beta_3$-targeted nanoparticles and all other controls, and Figs. 5 and 6 suggest that the entropy receiver may be more robust, much work remains to be done to demonstrate clinical utility. One encouraging fact is the ability to select operating parameters

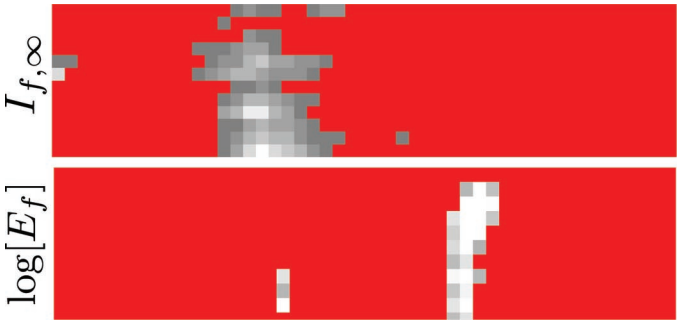

Fig. 6. A comparison of the confidence images, c, like that shown in Fig. 5, (top) for $I_{f,\infty}$ images with $c = 6.92$, and (bottom) $\log[E_f]$, images with $c = 9.55$. These thresholds were chosen as the minimum which produced no false positives in either of the control groups when analyzed by these signal receivers.

to preclude any false negatives from being detected within the treated group. Given that the spatial distribution of scatterers is likely to be significantly different between the control groups and the group injected with targeted nanoparticles, with nanoparticles in this group being concentrated in the advancing front of the tumor, it is possible that frequency filtering of the RF waveforms might be optimized for input to the $I_{f,\infty}$ receiver by high-pass filtering. In addition, utilization of a smoothing spline in place of the non-smoothing spline used in this study may yield improvements in the noise immunity of the $I_{f,\infty}$ receiver. These algorithms are being actively investigated in our group at this time.

References

[1] R. F. Wagner, S. W. Smith, J. M. Sandrik, and H. Lopez, "Statistics of speckle in ultrasound b-scans," *IEEE Trans. Sonics Ultrason.*, vol. 30, no. 3, pp. 156–163, May 1983.

[2] G. E. Sleefe and P. P. Lele, "Tissue characterization based on scatterer number density estimation," *IEEE Trans. Ultrason. Ferroelectr. Freq. Control*, vol. 35, no. 6, pp. 749–757, Nov. 1988.

[3] R. F. Wagner, M. F. Insana, and D. G. Brown, "Statistical properties of radio-frequency and envelope-detected signals with applications to medical ultrasound," *J. Opt. Soc. Am. A*, vol. 4, no. 5, pp. 910–922, May 1987.

[4] F. L. Lizzi, M. Ostromogilsky, E. J. Feleppa, M. C. Rorke, and M. M. Yaremko, "Relationship of ultrasonic spectral parameters to features of tissue microstructure," *IEEE Trans. Ultrason. Ferroelectr. Freq. Control*, vol. 34, no. 3, pp. 319–329, May 1987.

[5] K. D. Donohue, L. Huang, T. Burks, F. Forsberg, and C. W. Piccoli, "Tissue classification with generalized spectrum parameters," *Ultrasound Med. Biol.*, vol. 27, no. 11, pp. 1505–1514, Nov. 2001.

[6] P. M. Shankar, V. A. Dumane, T. George, C. W. Piccoli, J. M. Reid, F. Forsberg, and B. B. Goldberg, "Classification of breast masses in ultrasonic b scans using Nakagami and k distributions," *Phys. Med. Biol.*, vol. 48, no. 14, pp. 2229–2240, Jul. 2003.

[7] P. M. Shankar, "The use of the compound probability density function in ultrasonic tissue characterization," *Phys. Med. Biol.*, vol. 49, no. 6, pp. 1007–1015, Mar. 2004.

[8] K. V. Mogatadakala, K. D. Donohue, C. W. Piccoli, and F. Forsberg, "Detection of breast lesion regions in ultrasound images using wavelets and order statistics," *Med. Phys.*, vol. 33, no. 4, pp. 840–849, Apr. 2006.

[9] B. N. Maurizi, "Estimation of an entropy based functional," *Entropy*, vol. 12, no. 3, pp. 338–374, Mar. 2010.

[10] M. S. Hughes, J. N. Marsh, H. Zhang, A. K. Woodson, J. S. Allen, E. K. Lacy, C. Carradine, G. M. Lanza, and S. A. Wickline,

Authorized licensed use limited to: WASHINGTON UNIVERSITY LIBRARIES. Downloaded on July 21,2024 at 15:56:06 UTC from IEEE Xplore. Restrictions apply.

"Characterization of digital waveforms using thermodynamic analogs: detection of contrast-targeted tissue *in vivo*," *IEEE Trans. Ultrason. Ferroelectr. Freq. Control*, vol. 53, no. 9, pp. 1609–1616, Sep. 2006.

[11] M. S. Hughes, J. E. McCarthy, J. N. Marsh, J. M. Arbeit, R. G. Neumann, R. W. Fuhrhop, K. D. Wallace, D. R. Znidersic, B. N. Maurizi, S. L. Baldwin, G. M. Lanza, and S. A. Wickline, "Properties of an entropy-based signal receiver with an application to ultrasonic molecular imaging," *J. Acoust. Soc. Am.*, vol. 121, no. 6, pp. 3542–3557, Jun. 2007.

[12] M. S. Hughes, J. N. Marsh, J. M. Arbeit, R. G. Neumann, R. W. Fuhrhop, K. D. Wallace, L. Thomas, J. Smith, K. Agyem, G. M. Lanza, S. A. Wickline, and J. E. McCarthy, "Application of Renyi entropy for ultrasonic molecular imaging," *J. Acoust. Soc. Am.*, vol. 125, no. 5, pp. 3141–3145, May 2009.

[13] M. S. Hughes, J. E. McCarthy, M. V. Wickerhauser, J. N. Marsh, J. M. Arbeit, R. W. Fuhrhop, K. D. Wallace, T. Thomas, J. Smith, K. Agyem, G. M. Lanza, and S. A. Wickline, "Real-time calculation of a limiting form of the Renyi entropy applied to detection of subtle changes in scattering architecture," *J. Acoust. Soc. Am.*, vol. 126, no. 5, pp. 2350–2358, Nov. 2009.

[14] R. L. Wheeden and A. Zygmund, *Measure and Integral: An Introduction to Real Analysis*. New York, NY: Marcel-Dekker, 1977.

[15] W. H. Press, S. A. Teukolsky, W. T. Vetterling, and B. P. Flannery, *Numerical Recipes in C*, 2nd ed. Cambridge, UK: Cambridge University Press, 1992.

[16] D. L. Sackett, "Why randomized controlled trials fail but needn't: 2. Failure to employ physiological statistics, or the only formula a clinician-trialist is ever likely to need (or understand!)," *Can. Med. Assoc. J.*, vol. 165, no. 9, pp. 1226–1237, Oct. 2001.

Authorized licensed use limited to: WASHINGTON UNIVERSITY LIBRARIES. Downloaded on July 21,2024 at 15:56:06 UTC from IEEE Xplore. Restrictions apply.